

# Surface and Atmospheric Contributions to Passive Microwave Brightness Temperatures

Submitted by

Gail Skofronick Jackson  
Mesoscale Processes Branch  
NASA Goddard Space Flight Center  
Code 613.1, Bldg. 33, Rm. A416  
Greenbelt, MD 20771 USA  
301-614-5720, FAX 301-614-5492  
Gail.S.Jackson@nasa.gov

and

Benjamin T. Johnson  
University of Maryland, Baltimore County  
Joint Center for Earth Systems Technology  
Benjamin.T.Johnson@nasa.gov

Submitted to the Journal of Geophysical Research – Atmospheres  
April 30, 2010

*Abstract*— Physically-based passive microwave precipitation retrieval algorithms require a set of relationships between satellite observed brightness temperatures (TB) and the physical state of the underlying atmosphere and surface. These relationships are typically non-linear, such that inversions are ill-posed especially over variable land surfaces. In order to better understand these relationships, this work presents a theoretical analysis using brightness temperature weighting functions to quantify the percentage of the TB resulting from absorption/emission/reflection from the surface, absorption/emission/scattering by liquid and frozen hydrometeors in the cloud, the emission from atmospheric water vapor, and other contributors. The results are presented for frequencies from 10 to 874 GHz and for several individual precipitation profiles as well as for three cloud resolving model simulations of falling snow. As expected, low frequency channels (<89 GHz) respond to liquid hydrometeors and the surface, while the higher frequency channels become increasingly sensitive to ice hydrometeors and the water vapor sounding channels react to water vapor in the atmosphere. Low emissivity surfaces (water and snow-covered land) permit energy downwelling from clouds to be reflected at the surface thereby increasing the percentage of the TB resulting from the hydrometeors. The slant path at a 53° viewing angle increases the hydrometeor contributions relative to nadir viewing channels and show sensitivity to surface polarization effects. The TB percentage information presented in this paper answers questions about the relative contributions to the brightness temperatures and provides a key piece of information required to develop and improve precipitation retrievals over land surfaces.

## I. INTRODUCTION

Because precipitation is a critical link in the Earth's global water and energy cycles, there is an interest in retrieving precipitation (both rain and snow) in an accurate and consistent fashion on a global basis. The use of satellite observations, such as those available from the upcoming NASA Global Precipitation Measurement (GPM) mission, provides scientists with the necessary spatial and temporal coverage. Crucial for developing physically-based precipitation retrieval algorithms is an understanding of the physical relationships between satellite observations of the Earth and the state of the atmosphere and surface within the field of view. These characteristics are often interrelated, exhibiting complex spatial structures and temporal variations. Passive radiometer channels may respond to any medium within their field of view, including surface state and cloud conditions. The sensitivity to surface, temperature profiles, water vapor profiles, liquid hydrometeors, and ice hydrometeors varies depending on the channel frequency and satellite viewing angle. The lower frequency channels (10-37 GHz) are more sensitive to the surface and absorptive or emissive warming from liquid rain, while the higher frequency channels (85-874 GHz) are more sensitive to scattering from ice hydrometeors [e.g., *Evans et al.*, 2005]. Sounding channels near the water vapor absorption lines (23, 183, 325, and 448 GHz) respond primarily to the water vapor in the atmosphere and this absorption/emission continuum by water vapor generally increases with frequency. For hydrometeors, the amount, location, composition, and size distribution of the ice (and liquid) particles in the field of view produces varying brightness temperatures for different frequencies and permits retrievals of rain rates from 0.2 to 110 mm hr<sup>-1</sup> [*Hou et al.*, 2008].

Precipitation retrievals from space using channels from 10-183 GHz have become a mainstay in providing rainfall rate estimates globally as evidenced by the Tropical Rainfall

Measuring Mission (TRMM) [e.g., *Kummerow et al.*, 2000], the Advanced Microwave Scanning Radiometer – Earth Observing System (AMSR-E) [*Kawanishi et al.*, 2003], and the Advanced Microwave Sounding Units (AMSU-A and AMSU-B) [e.g., *Ferraro et al.*, 2005]. The Ku-band (13 GHz) radar aboard TRMM [*Kummerow et al.*, 1998] and the W-band radar aboard CloudSat [*Stephens et al.*, 2008] provide detailed limited-swath information about the vertical structure of cloud systems. The CloudSat radar responds primarily to cloud particles, light rain, and snow events, similar to high frequency (>90 GHz) passive radiometer channels.

The TRMM and AMSR-E radiometers with channels from ~10-89 GHz perform particularly well over oceans when used with physically based algorithms [*Lin and Hou*, 2008], while retrievals over land currently use empirical approaches [*Ferraro et al.*, 2005]. Compared to purely empirical / statistical methods, retrievals based on physical relationships are capable of providing a better understanding of the atmospheric and surface state being estimated given accurate knowledge of the necessary physical-radiometric relationships. Future retrievals over land, such as those for the NASA Global Precipitation Measurement (GPM) mission, are moving toward physically-based approaches, since these algorithms have worked well over oceans [e.g., *Kummerow et al.*, 2009].

Recently there has also been an increased interest in estimating both ice-phase precipitation particles (snow, graupel, etc.) above the melting layer and ice particles reaching the Earth's surface as snow in order to fully capture the atmospheric water cycle. Ice-phase precipitation detection and retrieval algorithms have been reported and shown to be useful in studying near-surface falling snow [*Skofronick-Jackson et al.*, 2004; *Ferraro et al.*, 2005; *Chen and Staelin*, 2003; *Kim et al.*, 2008; *Noh et al.*, 2009]. These falling snow precipitation retrieval algorithms include those that rely on neural networks, statistics, physical relationships, and/or

some combination thereof. The millimeter-wave and sub-millimeter-wave frequencies are especially sensitive both to the scattering and absorption/emission properties of ice particles, and these channels have been exploited in the above approaches.

The passive signature received by satellite radiometers from falling snow events tends to be small with respect to the other contributing factors to the observed brightness temperature. However, this signature increases as the channel frequency moves from the microwave to the sub-millimeter-wave regime. When the cloud has a liquid water path (LWP) of less than about 1 kg m<sup>-2</sup>, the surface can contribute more than 50% of the brightness temperature for frequencies below 37 GHz. Ideally, physically-based retrievals could correct for the surface contributions and eliminate more of the uncertainty due to it. Over oceans it is much easier to determine surface emissivity and temperatures since the surface is generally relatively uniform on the typical scales of passive microwave observations. On the other hand, the emissivity and temperature of the land surface exhibits much stronger variations than ocean, and precipitation (rain or snow) at the surface can exhibit a rapid and strong influence on these quantities as snow accumulates and rain wets soil and vegetation. To determine the sensitivity to variations in the physical relationships, the contributing factors to the brightness temperatures must be understood and explained. In this paper, we perform straightforward sensitivity analyses of the associated radiometric response for multiple physical realizations of the surface and clouds (rain, anvil, and falling snow events).

One approach that has been used to assist in determining the contributions from these various environmental parameters is Jacobian Decomposition [Voronovich and Gasiewski, 2004; Kim et al., 2008]. With Jacobians, a tangent linear relationship is created via the use of partial derivatives [e.g., Voronovich and Gasiewski, 2004]. The slopes of these partial derivatives can be

positive or negative depending on whether or not the brightness temperature increases or decreases in response to changes in the atmospheric variable of interest. Other approaches to investigating the sensitivity of brightness temperatures to atmospheric and surface contributors rely on information theory or optimal estimation theory [e.g., *English*, 1999; *Di Michele and Bauer*, 2006; *Bennartz and Bauer*, 2003; *L'Ecuyer et al.*, 2006]. These techniques are useful because they can be used to select the best possible instrument channels [*Di Michele and Bauer*, 2006], to assess the impact of uncertainties [*L'Ecuyer et al.*, 2006], and to determine the sensitivity of radiances to precipitation and atmospheric profiles [*Bennartz and Bauer*, 2003; *English*, 1999]. Our information content analysis approach employs the direct use of forward radiative brightness temperature (TB) calculations using the iterative or perturbation method [*Lenoble*, 1985] as opposed to the more commonly used adding/doubling method.

The advantage of the iterative method for computing passive microwave TBs is that it provides temperature weighting functions that can be used to show the relative contributions from the combined extinction (absorption plus scattering) for the physical cloud parameters of each level in the atmosphere and for the top-of-atmosphere and surface boundaries. The temperature weighting function serves as a factor to multiply the physical atmospheric temperature in order to compute TB values [e.g., *Gasiewski*, 1993]. In this research, the temperature weighting function concept is exploited to analyze the TB sensitivity to the surface, atmospheric hydrometeors, the atmospheric water vapor, and other remaining constituents. In the numerical analysis, an estimate of the TB contribution (in Kelvin) from each of these cloud and surface characteristics is determined, so that the sum of these various parts equals the computed brightness temperature. The key benefit of this type of analysis is to be able to easily separate

contributions to the brightness temperatures from the physically distinct and measureable quantities in each layer of the atmosphere.

This paper determines the relationships between the key physical variables that influence passive microwave observations. We perform these analyses for selected frequencies ranging from 10 to 874 GHz, consistent with current and planned passive microwave sensors (e.g., AMSR-E, TRMM, AMSU-B, *Buehler et al.*, [2007]). This investigation probes the TB sensitivity over several cloud classifications, such as individual profiles of convective rain, falling snow, anvil ice, as well as cloud resolving model (CRM) simulations of three snow events. Vertical atmospheric profile structures from these various cloud classifications are used as input for a robust radiative transfer model [*Skofronick-Jackson et al.*, 2004] where nadir and 53° viewed brightness temperatures are calculated. Section II describes the different case profiles, while Section III provides the procedure for computing brightness temperatures and decomposing them into quantitative percentage contributions from each source. The results for the TB and temperature weighting vectors are discussed in Section IV and Section V describes the percentage analysis results. A summary and conclusions are presented in Section VI.

## II. SELECTION OF CASE PROFILES

While many representations of global precipitation would provide statistical results of the surface and atmospheric contributions to brightness temperature values, such results would also be diluted by the wide variety of precipitation events across the globe in all seasons and latitudes. To focus on a few key cases allows the detailed analysis needed for understanding the specifics of how surface and cloud conditions affect the resultant brightness temperature values. This information can eventually be applied in a general sense. Due to the upcoming GPM mission's interest in the retrievals of falling snow, we emphasize snow events herein. Thus, three cloud resolving model (CRM) simulations of snow events, and six individual profiles of rain and falling

snow over both land and ocean were selected for analysis. The CRM cases allow averaging over multiple profiles of snowing events, while the individual cases allow a closer examination of specific rain, snow, and anvil cases. The CRM cases included an MM5 simulation of the 5-6 March 2001 New England blizzard [Skofronick-Jackson *et al.*, 2004; Kim *et al.*, 2008] and a WRF simulation of the 20-22 January 2007 winter precipitation events located near the Great Lakes region [Shi *et al.*, 2010]. Figure 1a shows the ice water path (IWP) image of the March 2001 CRM case that deposited up to 75 cm of snow in Vermont, USA. The WRF simulation encompassed two events: (1) a shallow cloud lake effect snow on 20 January 2007 (Fig. 1b) with localized snow accumulations of ~30 cm along the snow bands, and (2) a synoptic snow event on 22 January 2007 (Fig. 1c) with widespread snow accumulations of 5-6 cm. More complicated cases of wet/melting snowfall, multi-level clouds, and 3-D geometry effects were excluded from this analysis.

The individual cases analyzed include heavy rain over ocean, light rain over land, anvil (non-precipitating) hydrometeors over ocean, light falling snow over land, moderate falling snow over land, and heavy falling snow over land. The heavy rain, light rain, and anvil cases come from an MM5 model run of Hurricane Erin [Wu *et al.*, 2006]. The heavy rain case was an average of 56 MM5 profiles with surface rain rates of  $25 \pm 0.2 \text{ mm hr}^{-1}$ , while the light rain case was an average of 448 MM5 profiles with surface rain rates of  $0.5 \pm 0.2 \text{ mm hr}^{-1}$ . The anvil case was generated from the MM5 Hurricane Erin simulation by eliminating all profiles with rain, snow, or graupel particles between 0 and 7 km, and then by selecting only profiles with  $\Sigma(\text{snow} + \text{graupel} + \text{cloud ice})$  above 7km to be greater than  $0.12 \text{ g m}^{-3}$  and this led to averaging over 51 profiles. The heavy snow case was determined by selecting the profile with the maximum surface snow+graupel water content (with LWP = 0) from the profiles in the MM5 cloud



simulation for the 5-6 March 2001 New England blizzard, the moderate and light snow cases are a variation of the heavy snow case as described below.

The vertical profiles of hydrometeors, temperature, and relative humidity for the anvil, heavy rain, light rain, heavy snow, and light snow cases are shown in Figure 2. The heavy snowing case transitions nearly linearly with respect to height from  $0.0 \text{ g m}^{-3}$  at the  $\sim 10\text{km}$  top of the cloud to  $0.82 \text{ g m}^{-3}$  at the surface. If we assume the *Marshall-Palmer* [1948] particle size distribution to convert the surface snow content into a melted rain rate (e.g.,  $RR = 19.9M^{1.2}$ ), the RR for this profile is  $15.7 \text{ mm hr}^{-1}$  or approx 6 inches an hour of a fluffy snow rate (see Table I) assuming  $1 \text{ m s}^{-1}$  vertical velocity and 10-to-1 ratio of fluffy snow pack to melted depth. The snowfall rate will change if the snow is considered to be more or less dense than the commonly assumed 10-to-1 conversion or if the vertical velocity changes. To reduce this heavy snowfall rate into moderate and light snow rate cases, the entire vertical profile contents were multiplied by 0.21 and 0.07 to obtain surface non-melted snowfall rates of  $25 \text{ mm hr}^{-1}$  and  $6.25 \text{ mm hr}^{-1}$  respectively (Table I).

In order to perform the numerical radiative transfer, the information required for each case includes the cosmic background temperature, all surface inputs (surface skin temperature and emissivity), all atmospheric inputs (e.g., vertical profiles of particle size distributions, ice particle shapes and ice-air-water densities, temperature, and water vapor amounts). The simulation cases obtain most of this information as part of the CRM output. Five cloud particles are allowed in the radiative transfer calculations: non-precipitating cloud water, non-precipitating cloud ice, and precipitating rain, snow, and graupel. The non-precipitating particles are monodisperse Rayleigh particles with fixed particle size and the number density varying to account for the total hydrometeor content per layer. For the hydrometeor particle size distributions, liquid rain particles

were assumed to have spherical shapes and to follow the *Marshall-Palmer* [1948] particle size distribution. For the ice particles, non-spherical particles from G. Liu's database [2004] were used. For the snow particles a relatively sparse dendritic shape was assumed (Figure 3a). For the graupel particles the denser 6-sided bullet rosette was assumed (Figure 3b). Both the dendrite snow and six-bullet graupel were considered randomly oriented with no polarized contributions. The *Sekhon-Srivastava* [1970] particle size distribution (PSD),  $N(D) = N_0 \exp(-\Lambda D)$ , was used to obtain the  $\Lambda$  parameter in the exponential PSD.  $N_0$  was chosen such that ice water content (IWC) was preserved for each layer, with integration over size limited to the fixed minimum and maximum particle sizes within Liu's non-spherical database [Liu, 2004].

The boundary conditions for the top of the atmosphere and the surface must be prescribed prior to brightness temperature computations and analysis. For all cases, the top of the atmosphere was assumed to be 2.7 K, the cosmic background temperature. The near-surface features of precipitation rate, surface temperature, surface conditions, and relative humidity for these individual cases are presented in Table I along with the liquid water path (LWP) and ice water path (IWP). For the heavy rain and anvil cases, calculations were performed over a calm ocean surface where surface emissivity could be computed using Fresnel relations [Gasiowski, 1993]. For the light rain case, a surface emissivity of 0.98 was assumed for all frequencies over forested regions following *Hewison* [2001], while for the individual snowing cases the surface was assumed to be deep dry snow with an emissivity of 0.82 for 10 GHz, 0.72 for 19 GHz, 0.70 for 21 GHz, 0.63 for 37 GHz, 0.64 for 89 GHz, 0.72 for 166 GHz, 0.80 for 183 GHz and higher frequencies as provided by *Hewison and English* [1999].

The surface characteristics for the MM5 and WRF models were provided by the simulations and included land surface temperature, land type, and snow depth. The land type and

snow depth of the CRM outputs was used to prescribe the emissivity of the surface. The base emissivities ( $\epsilon_{\text{base}}$ ) for CRM land type classifications of urban, crop, grass, forest, and water were classified as bare soil, close stubble, close grass, evergreen forest, and water, respectively and taken from *Hewison* [2001]. Because the WRF and MM5 models provide snow depth (SD) in cm as an output parameter, it was used to adjust the emissivities by the deep dry snow emissivities ( $\epsilon_{\text{snow}}$ ) listed above for the individual snow profile cases using:

$$\epsilon_{\text{adj}} = \frac{\text{SD}}{30} \epsilon_{\text{snow}} + \left(1 - \frac{\text{SD}}{30}\right) \epsilon_{\text{base}} \quad (1)$$

Here, a 30 cm threshold is use to indicate that all low vegetation is covered by snow such that the  $\epsilon_{\text{snow}}$  is used. For SD greater than 30 cm, only  $\epsilon_{\text{snow}}$  is used. Since the Hewison and English emissivities were derived for localized conditions using aircraft measurements and because generally there is much variability in the emissivity, a random emissivity component of  $\pm 0.02$  was added to the prescribed emissivities for each profile in the WRF and MM5 domains. These TB calculations are performed at the native resolution of the simulations (1km for WRF, 4km for MM5) and for each of the 207,000 and 53,000 profiles in the WRF and MM5 domains, respectively.

### III. PROCEDURE

In order to determine the percentage contributions from the surface, atmospheric hydrometeors and water vapor components of these case study clouds, a procedure to extract the separate contributions is employed. The procedure requires the use of a forward radiative transfer (FRT) model to compute brightness temperatures (TBs). During the computations, temperature weighting vectors are generated and then used to extract out the contributions from the atmospheric and surface components.

#### A. Radiative Transfer Calculations

The radiative transfer equations rely on the planar-stratified, multiple scattering based model described in [Skofronick-Jackson *et al.*, 2004]. For ease in understanding the relationships, nadir brightness temperatures are the focus and presented first, followed by results at 53°. When the TBs are computed, temperature weighting functions [Gasiewski, 1993] are obtained. The brightness temperature at each frequency is the integrated sum over all heights of the product of the weighting vector value and the atmospheric temperature plus the contributions from the ground and cosmic background temperatures:

$$\mathbf{TB} = \int_0^\infty T(z) \mathbf{W}(z) dz = T_0 \mathbf{W}_0 + T_{CB} \mathbf{W}_{CB} + \sum_{i=1}^I T(z_i) \mathbf{W}_{ALL}(z_i) \Delta z_i \quad (2)$$

where the subscripts 0 (at  $z_i = 0$ ), and  $CB$  denote ground surface and cosmic background, respectively,  $T(z_i)$ ,  $\mathbf{W}_{ALL}(z_i)$  denote the atmospheric physical temperature in Kelvin and weighting vector value in units of  $\text{km}^{-1}$ , respectively, for level  $i$  of the cloud profile that consists of  $I$  total levels, and  $\Delta z_i$  is the height increment between level  $i$  and level  $i-1$ . The brightness temperature contributions (in Kelvin) from level  $i$  are the product  $T(z_i) \mathbf{W}_{ALL}(z_i) \Delta z_i$ . The weighting vectors depend on the atmospheric cloud constituents at each layer in the atmosphere. The weighting vectors  $\mathbf{W}_{ALL}$ ,  $\mathbf{W}_0$ , and  $\mathbf{W}_{CB}$  are defined in Gasiewski [1993] where  $\mathbf{W}_{ALL}$  is denoted  $\mathbf{W}^{(n)}$ . When plotted the temperature weighting functions show that the different frequencies respond to different vertical layers and cloud components (e.g., Gasiewski [1993], Skofronick-Jackson, *et al.*, [2004]).

#### B. Weighting Vector Decomposition and Percentage Computation

The  $\mathbf{W}_{ALL}$  weighting values include the effects of every component of the vertical profile, e.g., liquid and frozen precipitating hydrometeors, non-precipitating cloud water and cloud ice, water

vapor, nitrogen, and oxygen. From Eqn. 2, the surface (S) contribution is simply  $T_0 \mathbf{W}_0$ , while the cosmic background (CB) contribution is  $T_{CB} \mathbf{W}_{CB}$ . It is possible to obtain absorption-only analytical weighting function expressions (e.g., for water vapor in cloud free atmospheres as in *Jackson and Gasiewski, 1995*) in addition to the temperature weighting functions in Eqn1, when scattering is present analytical weighting functions for components such as precipitating hydrometeors become intractable. Therefore the approach taken here is to post-process the temperature weighting function  $\mathbf{W}_{ALL}$  (which accounts for the vertical atmospheric and cloud features) by decomposing it into separate quantitative components for studying the relative contributions from the precipitating hydrometeors (P), the non-precipitating cloud water and cloud ice (CWCI), the water vapor (RH), and other contributions ( $N_2$ ,  $O_2$ , etc) using the following expression:

$$\mathbf{W}_{ALL}(z_i)T(z_i) = M_P(z_i)\mathbf{W}_P(z_i) + M_{CWCI}(z_i)\mathbf{W}_{CWCI}(z_i) + RH(z_i)\mathbf{W}_{WV}(z_i) + \mathbf{W}_{other}(z_i)T(z_i) \quad (3)$$

where M denotes the liquid or ice water content of the subscripted variable and  $RH(z_i)$  is the relative humidity at height  $z_i$ . This post-processing decomposition defines  $\mathbf{W}_P$ ,  $\mathbf{W}_{WV}$ ,  $\mathbf{W}_{CWCI}$ , and  $\mathbf{W}_{other}$  by simply renormalizing  $\mathbf{W}_{ALL}$  using the various extinction coefficients:

$$\mathbf{W}_P(z_i) = \frac{\mathbf{k}_{Pext}(z_i) T(z_i) \mathbf{W}_{ALL}(z_i)}{\mathbf{k}_{ext}(z_i) M_P(z_i)} \quad (\text{K km}^{-1} \text{ m}^3 \text{ g}^{-1}) \quad (4)$$

$$\mathbf{W}_{CWCI}(z_i) = \frac{\mathbf{k}_{CWCI}(z_i) T(z_i) \mathbf{W}_{ALL}(z_i)}{\mathbf{k}_{ext}(z_i) M_{CWCI}(z_i)} \quad (\text{K km}^{-1} \text{ m}^3 \text{ g}^{-1}) \quad (5)$$

$$\mathbf{W}_{WV}(z_i) = \frac{\mathbf{k}_{WV}(z_i) T(z_i) \mathbf{W}_{ALL}(z_i)}{\mathbf{k}_{ext}(z_i) RH(z_i)} \quad (\text{K km}^{-1} \%^{-1}) \quad (6)$$

$$\mathbf{W}_{other}(z_i) = \frac{[\mathbf{k}_{O_2}(z_i) + \mathbf{k}_{N_2}(z_i)] \mathbf{W}_{ALL}(z_i)}{\mathbf{k}_{ext}(z_i)} \quad (\text{km}^{-1}) \quad (7)$$

where

$$\mathbf{k}_{ext}(z_i) = \mathbf{k}_{Pext}(z_i) + \mathbf{k}_{WV}(z_i) + \mathbf{k}_{CWCI}(z_i) + \mathbf{k}_{O_2}(z_i) + \mathbf{k}_{N_2}(z_i). \quad (8)$$

The  $\mathbf{k}_{Pext}$  term is the hydrometeor extinction coefficient (the sum of the absorption and scattering coefficients for the rain, snow, and graupel precipitating hydrometeors for layer  $z_i$ ),  $\mathbf{k}_{CWCI}$  is the sum of the extinction coefficients for cloud water and cloud ice,  $\mathbf{k}_{WV}$  is the extinction coefficient for water vapor, and  $\mathbf{k}_{O_2}$  and  $\mathbf{k}_{N_2}$  are the extinction coefficients for  $O_2$ , and  $N_2$ . Note that  $\mathbf{k}_{ext}$  is also used non-linearly in integrals while computing  $\mathbf{W}_{ALL}$  (which is one reason analytical solutions for scattering weighting functions don't yet exist). This means that  $\mathbf{W}_P$ ,  $\mathbf{W}_{CWCI}$ ,  $\mathbf{W}_{WV}$  and  $\mathbf{W}_{other}$  are minimally contaminated by the total  $\mathbf{k}_{ext}$  from the overall constituents, however, the majority of the response is captured for each weighting function component and the renormalization serves to elucidate the relationships between brightness temperatures and the underlying cloud and surface features..

Another point to clarify is that a large  $\mathbf{k}_{Pext}$  term can be caused by a large absorption coefficient and/or a large scattering coefficient. In radiative transfer, large scattering coefficients typically result in an upwelling brightness temperature received by a satellite radiometer that is colder than in a non-scattering medium. The advantage of using this weighting function analysis is that it captures percentage contribution information from large scattering coefficients regardless of the reductions in brightness temperature. Figure 4 gives representative absorption and scattering coefficients for fixed values of hydrometeor IWC (0.01, 0.1, 0.5, and 0.75 g m<sup>-3</sup>) for five particle types (rain; the Liu dendrites, the Liu 6-bullet rosettes, and for comparison fluffy snow spheres (10% ice, 90% air) and solid snow spheres). These contents span the range of contents found in the vertical layers of the selected precipitation cases. Fig. 4 shows that liquid rain has a high

absorption coefficient across all frequencies, whereas the absorption coefficients for the frozen hydrometeors are 1 to 3 orders of magnitude smaller. The scattering coefficients for the various hydrometeors are similar for the 0.1, 0.5, and 0.75 g m<sup>-3</sup> cases (Figs. 4b-d). For the 0.01 g m<sup>-3</sup> case (Fig. 4a), the amount of ice in the frozen layer is too small to cause appreciable scattering whereas the rain does cause an order of magnitude larger scattering coefficient (but two orders of magnitude smaller than the higher content cases). Note also that the 6-bullet rosette, our “graupel” particle, has more scattering than the dendrite particle, our “snowflake” particle. One would expect that denser graupel generates more scattering than fluffy snowflake particles, and helps to justify our choice of these shapes for our snow and graupel particles.

Once the temperature weighting vectors have been decomposed into contributions from the surface, cosmic background, atmosphere (precipitating and non-precipitating particles), and RH they can be used to obtain the value of the TB resulting from each of these components:

$$TB_{surf} = T_0 \mathbf{W}_0 ; \quad TB_{CB} = T_{CB} \mathbf{W}_{CB} \quad (9)$$

$$\mathbf{TB}_{Prec} = \sum_{i=1}^I T(z_i) \mathbf{W}_P(z_i) \quad (10)$$

$$TB_{CWC} = \sum T(z_i) \mathbf{W}_{CWC}(z_i) \quad (11)$$

$$\mathbf{TB}_{RH} = \sum_{i=1}^I T(z_i) \mathbf{W}_{WV}(z_i) \quad (12)$$

In turn, the percentages are obtained by dividing the above numbers by the total TB defined in Eqn. 2, with the remainder percentage due to oxygen, nitrogen and other components.

#### IV. TEMPERATURE WEIGHING VECTOR AND BRIGHTNESS TEMPERATURE RESULTS

The temperature weighting vectors (Eq. 2, Figure 5) are used to investigate what parts of the atmosphere and boundary features contribute to the computed brightness temperature. A larger magnitude weight in  $\mathbf{W}_{ALL}(z_i)$  caused by a larger magnitude extinction coefficient indicates an increased contribution from the atmosphere at those  $z_i$  height levels. For example, in Figure 5 for the heavy snow rate case, the magnitude of the nadir-viewed 89 GHz channel is approximately 12 K km<sup>-1</sup> at the 1-2 km height levels, whereas 166 GHz peaks at 2-4 km with weights of ~25K km<sup>-1</sup> and the 183 to 874 GHz channels have larger magnitude peaks (30-40K km<sup>-1</sup>), but at higher altitudes. Note that the weighting vectors are distributed across the vertical extent of the cloud indicating that the TB values are an integrated quantity over the height.

When comparing the weighting functions of the heavy and light rain and anvil cases there are some similarities (e.g., lower frequencies probe to the near Earth atmospheric levels while higher frequencies are more sensitive to the upper altitudes of a cloud). There are also differences due to the amount and distribution of the hydrometeors within the clouds for the various cases. The vertical extent of the weighting function is dependent on the underlying cloud; lower LWP causes the vertical extent to be broadened (e.g., compare 89 GHz for heavy and light rain). Tracing the 183±7 GHz channel weighting functions across all of the individual cases plotted in Figure 5 shows that the weighting function peaks closer to the surface when the integrated quantity of hydrometeors is smaller (e.g., anvil and snow cases). This same phenomenon occurs with the 325, 448, 642, and 874 GHz channels.

Using the forward RT procedure, the resultant brightness temperatures for the six cases are computed and provided in Table II. This table shows the nadir brightness temperatures when each of the six profiles has the original hydrometeor profile as seen in Figure 2 and when all hydrometeors are zeroed out. The weighting function profiles and brightness temperature values



are not provided for the WRF and MM5 cases since they are composed of more than 207,000 and 53,000 profiles respectively.

Looking at the liquid rain cases, Table II shows that for the heavy rain over ocean case, the 10, 19, and 21 GHz channel clear-air brightness temperatures respond strongly when liquid raindrops are introduced over ocean surfaces (100K differences). The emission from the raindrops warms the TBs with respect to the radiometrically cooler ocean surface background. There is also a strong TB cooling ( $\sim 60$ -100K) due to scattering from ice aloft in the 89 GHz and higher channels. For the light rain over land case, there is little to no sensitivity at 10-37 GHz with respect to clear air because there are few liquid hydrometeors in the lower part of the cloud and a much lower LWP (Table I). At 89 GHz and higher, again there is sensitivity and cooling due to ice scattering with 20-30K differences. The cooling due to scattering from ice at 89, 166, and the 183 GHz channels is a good indicator of light rain over land. Because the anvil case has smaller ice particles at higher altitudes, only the highest channels ( $\geq 325$  GHz) respond with any significant change with respect to the clear air brightness temperatures.

The TB values associated with the snowing cases in Table II show that for frequencies between 10 and 89 GHz, there is less than a 15K difference between the heavy, moderate, and light snow, and clear air brightness temperature values. This means that these channels are nearly insensitive to falling snow at these rates and for these cloud profiles. As the frequency increases, there is greater sensitivity to falling snow particles: At 166 GHz, there is a 48K difference between clear air and the heavy snow case, but the differences are insignificant between clear air and the moderate and light snow cases. The  $183 \pm 7$  GHz channel are sensitive ( $\sim 35$ K) to the deep (10km tall) heavy snow clouds. The 325, 642, and 874 GHz channels show strong sensitivity to falling snow (e.g., at 325 GHz the TB show a nearly 50K differential between the heavy snow and

clear air cases). Between the clear air case and the light snow case for all channels the TB differences are less than 5K and less than 10K between the moderate and clear air cases.

Given the low sensitivity for the moderate snow and especially the light snow cases for current satellite channels, thresholds of retrieval detection and estimation will be dependent on the snowing cloud being observed and available ancillary data. Also, since during retrievals one does not know the true state of the surface, nor the cloud microphysics, there are additional unknowns that can cause errors. Specifically, at 89 GHz, each 0.1 increment in surface emissivity error causes a 25 K change in brightness temperature for clear air profiles (Figure 6). Similarly, for a fixed surface emissivity, an error of 10°C for specifying the land surface skin temperature (effective emitting temperature) can cause a 2-3 K change in the TB values. As expected, Fig. 6 shows that the surface characterization has a large impact on brightness temperature values, especially for clear-air or nearly clear-air conditions for window channels at 10, 37, 89 and 166 GHz. The figure also shows that the 183 GHz channels are less sensitive to surface features due to their sensitivity to water vapor in the profile.

## V. PERCENTAGE ANALYSIS

By piecing together the contributions from the precipitating hydrometeors within the cloud, the atmospheric water vapor and the surface, we can have a better understanding of how all the components work together to produce a brightness temperature related to the storm scenario. Eqns. 10, 11, and 12 provide the basis for determining the percentages for the six individual and 3 simulated cases as reported in Figures 7-10. The percentage of the brightness temperature resulting from the cosmic background for the individual cases is not shown in the figures, but is no more than 1.3% (at 10 GHz for the anvil case) and is closer to 0.0-0.3% for the other channels.

Figure 7 shows the percentage contributions for the heavy rain, light rain, and anvil cases. For the heavy rain case (Fig. 7a) the hydrometeors (liquid rain and frozen hydrometeors) provide more than 50% of the brightness temperature value. For channels at  $183\pm 1$  and  $448\pm 1$  GHz, the water vapor is a strong contributor to the brightness temperatures. It is only at 10 GHz where the surface significantly contributes ( $\sim 35\%$ ) to the brightness temperature. For the light rain case (Fig. 7b), the hydrometeors contribute less than for the heavy rain case (because their integrated quantity is less than that of the heavy rain). As such, the surface contributes more than 70% for all frequencies less than 89 GHz. We also note that there is an increasing contribution from the non-precipitating cloud water and cloud ice as the channel frequency increases.

To explore the differences between heavy rain over ocean versus over land, the FRT calculations were performed with the heavy rain case over the same land background (forested) as used for the light rain case. When these percentage contributions were compared to the heavy rain over ocean, the most distinct change was at 10 GHz, where the contribution from the hydrometeors was greater for the ocean case than the land heavy rain case (33% hydrometeor contribution from land case versus a 62% hydrometeor contribution from the ocean case). This is due to the reflective surface of water (lower emissivities) which permits energy downwelling from hydrometeors in clouds to be reflected at the surface and included in the brightness temperature as measured from an aircraft or satellite. This is an important finding since snow covered surfaces also have more reflective surfaces, and this fact will need to be accounted for in any FRT of retrievals of precipitation over snow-covered surfaces.

For the anvil case in Fig. 7c, at low frequencies that are typically sensitive to the liquid drops (which don't exist in the anvil case) the brightness temperatures are more sensitive to the surface. At higher frequencies the anvil percentages due to the water vapor in the profile are 50-

90% and at the highest frequencies (642 and 874 GHz) the percentages due to the hydrometeors are nearly 10-40% because these channels are especially sensitive to small ice particles as seen in anvil clouds [Evans *et al.*, 1998; Evans *et al.*, 2005].

In Table III, the percentage contributions for the surface, hydrometeors and relative humidity are provided for radiative transfer at a  $53^\circ$  viewing angle. Note that these percentages do not add to 100% because the contributions from CWCI, O<sub>2</sub>, N<sub>2</sub>, and cosmic background are not presented. In this table, the largest differences at  $53^\circ$  are at the lower frequencies where the oceanic surface polarizations affect the TB values at vertical (V) and horizontal (H) polarizations, while at higher frequencies the surface polarization percentages do not change because these channels are not sensitive to the surface. The V and H polarization percentages of the light rain case are equivalent because there is no surface polarization for land. Furthermore the non-spherical snow and graupel are randomly oriented such that they do not contribute to polarized TB values. Comparing these percentages to those in Figure 7 (for nadir viewing) there is a slight increase in the percentages from the precipitating hydrometeors and RH for the V & H percentages because of an increase in slant path for the  $53^\circ$  viewing angle calculations.

For Figure 8, which shows the percentage contributions for the heavy, moderate, and light snow cases, there is a progression of decreasing percentages from the hydrometeors as the snowing rates decrease. Figure 8a, shows the percentages due to hydrometeors range from 20 to 90% for the heavy snow case (channels 89 to 874 GHz). For the moderate snow case (Fig. 8b) at these frequencies, the hydrometeor percentages are between 5 and 30%, whereas for the light snow case (Fig. 8c), the percentages from the hydrometeors drop to 1 to 10%. There is a corresponding increase in the percentages from water vapor in the cloud. Not surprisingly, as shown in Fig. 8 for the snowing profiles (non-raining cases), the contributions for channels 10 to

89 GHz show a significant percentage from the surface. Figure 4 gives a key piece of information as to why there is less of a contribution from the hydrometeors (and more from the land) when only frozen hydrometeors are present in the profile. Figure 4 shows that the absorption and scattering of rain is higher than that of frozen particles for frequencies up to 100 GHz. Thus when liquid particles are present, the  $K_{Pext}$  term in Eqn. 4 is high and hence the value of  $TB_{prec}$  in Eqn. 11 is elevated.

Table IV provides the percentages for the snowing cases. The nadir-viewing angle percentages are those that appear in Fig. 8. These nadir viewed values are compared to the 53° angle percentages. Since the land surface component and randomly oriented snow particles have no polarization dependence, the V and H percentages are not different and only one is shown in Table IV. The 53° viewing angle results show a slight increase in percentages from the hydrometeors with corresponding decreases in surface percentages and RH percentages. This slight increase in percentages from the hydrometeors is due to the increased slant path at 53°.

Figure 9 provides the percentages for the WRF 20 January 2007 lake effect snow case (panel a) and the 22 January 2007 synoptic snow case (panel b). In order to partition the percentage results for the 207,000 profiles within each of the WRF CRM simulation, an average was taken only over those profiles with IWP of 0.5 to 1.0 kg m<sup>-2</sup> (18,160 profiles for 20 January 2007 and 71,420 profiles for 22 January 2007). We can then intercompare the lake effect case to the synoptic case to illuminate any differences in percentage based on the structure of the vertical profiles. Thus comparing Fig. 9a (lake effect) to Fig. 9b (synoptic), the most noticeable differences are for channels 166, 183, and 325 GHz where the synoptic snow event case is less sensitive to the surface and more sensitive to the snow particles. This is likely because the lake effect events are shallow (3 to 4 km) clouds, whereas the synoptic events are 6 to 7 km tall. Thus,

despite both plots being averaged over the 0.5 to 1.0 kg m<sup>-2</sup> IWP, the taller clouds impact the weighting functions over a larger vertical extent than the shallower clouds.

Finally, in Figure 10 the percentages from the MM5 heavy blizzard case are shown. For this case, percentages for an IWP of 0.5 to 1.0 kg m<sup>-2</sup> (5325 profiles averaged, Fig. 10a) and for an IWP of 9.5 to 10.0 kg m<sup>-2</sup> (5 profiles averaged, Fig. 10b) were plotted. At low frequencies, the dominating factor is evident by the high percentages from the surface for all cases shown in Figure 10 (i.e., there is no liquid water to affect low frequency TB values). Since this is a deep snowing cloud (to ~10 km altitude) there is both a greater effect from water vapor in the cloud (for those water vapor channels of 183, 325, and 448 GHz) and a greater effect from hydrometeors in the profile. Thus there are competing factors that modify the percentages from the snow in the profile and the water vapor in the profile. A detailed analysis to determine the thresholds of detection for falling snow cases needs to be undertaken to link TB depressions to the underlying falling snow event characteristics (e.g., cloud top, IWP, particle sizes and shapes, water vapor profile, etc.).

## VI. CONCLUSIONS

This work has provided an analysis method to determine the contributions to brightness temperature values from surface emission, from atmospheric cloud hydrometeors, from cloud water plus cloud ice, from the water vapor within the vertical profile, from the cosmic background, and from O<sub>2</sub> and N<sub>2</sub>. This analysis was performed for nadir-viewing and 53° viewed observation channels spanning 10 to 874 GHz, including both window and water vapor sounding channels. These channels are relevant to current and confirmed future missions as well as channels yet to be approved for a satellite mission. Figs 7-10 show the percentage of the brightness temperature values resulting from the various contributing factors for several

individual profile cases (heavy rain over ocean, light rain over land, anvil over ocean, heavy snow over land, moderate snow over land, and light snow over land) as well as for the average percentages resulting from three cloud resolving model simulations (for a lake effect snow event, a synoptic snow event, and the 2001 New England blizzard). Across all these cases several key points became evident:

- 1) The low frequency channels (<89 GHz) are extremely sensitive to the surface (with > 40% contribution to the TBs) except in the presence of high LWP (e.g., heavy rain cases).
- 2) The sounding channels have a large contribution from the water vapor in the vertical profile, when there is a limited quantity of hydrometeors in the profile.
- 3) The higher frequency channels (both sounder and window channels) are sensitive to the frozen hydrometeors in the cloud.
- 4) Low emissivity surfaces (water and snow-covered land) permit energy downwelling from hydrometeors in clouds to be reflected at the surface and therefore increase the percentage of the brightness temperature resulting from the hydrometeors.
- 5) The type and vertical structure of a snow event (e.g., lake effect, synoptic, blizzard) affects the percentages resulting from the surface and hydrometeors.
- 6) The slant path at a 53° viewing angle increases the percentage contributions from hydrometeors relative to nadir viewing channels and the percentages from the surface show sensitivity to surface polarization effects.

This work provides quantitative percentage values of the sources of brightness temperature signals and corroborates earlier investigations indicating that low frequency channels (<90 GHz) are sensitive to the surface and liquid particles, and that the high frequency channels are sensitive

to frozen particles and to atmospheric water vapor. These relationships are complicated, non-linear, and vary for each channel and remotely sensed precipitation event. The number of degrees of freedom in the physical state of precipitation events is larger than the degrees of freedom available from remotely sensed observations (for current and near future platforms). Thus for retrievals over land that are physically based, ancillary data will be extremely useful in reducing the unknowns and assumptions. Primarily, information about the surface emission as well as the vertical temperature and water vapor profiles are needed. It is probable that numerical weather prediction models can provide adequate vertical information. On the other hand, surface emission may require concentrated research and modeling efforts especially over certain surfaces (e.g., snow covered surfaces and deserts). While awaiting globally accurate models of surface emission, other approaches might include statistical analysis of climatological emissivities, retrievals of emissivity during clear air overpasses (with dynamic modeling of the surface as it rains or snows), or even assuming that clear air brightness temperatures just prior to a precipitation event represent the contributions from these environmental conditions. Since surface emission plays a large role for the typical frequencies used for precipitation sensors (10 to 183 GHz), future work should focus on obtaining realistic and validated surface emission globally as concurred by *Noh et al.*, [2009]. Nevertheless, the results presented herein are useful for retrieval algorithm development for upcoming missions such as GPM, especially over land surfaces and for falling snow events.

#### ACKNOWLEDGMENTS

Dr. W.-K. Tao is thanked for generating and providing the WRF model simulation and Dong-Eon Chang is thanked for the MM5 simulation. We thank Dr. Gousheng Liu for providing the non-spherical ice particle scattering database. This work was supported by Ramesh Kakar at NASA Headquarters through Precipitation Measurement Mission funding.



- Bennartz, R., and P. Bauer (2003), Sensitivity of microwave radiances at 85–183 GHz to precipitating ice particles, *Radio Sci.*, *38*(4), 8075, doi:10.1029/2002RS002626.
- Bueher, S. A., C. Jimenez, K. F. Evans, P. Ericksson, B. Rydberg, A. J. Heymsfield, C. J. Stubenrauch, U. Lohmann, E. Emde, V. O. John, T. R. Sreerekha, and C. P. Davis (2007), A concept for a satellite mission to measure cloud ice water path, ice particle size, and cloud altitude, *Q. J. R. Meteor. Soc.*, *133*, 108–128.
- Chen F. W. and D. H. Staelin (2003), AIRS/AMSU/HSB precipitation estimates, *IEEE Trans. Geosci. Remote Sens.*, *41*, 410–417.
- Di Michele, S. and P. Bauer (2006), Passive microwave radiometer channel selection based on clouds and precipitation information content, *Q. J. R. Meteorol. Soc.*, *132*, 1299–1323.
- English, S. J., (1999), Estimation of temperature and humidity profile information from microwave radiances over different surface types, *J. Appl. Meteor.*, *38*, 1526–1541.
- Evans, K. F., S. J. Walter, A. J. Heymsfield, and M. N. Deeter, (1998), Modeling of submillimeter passive remote sensing of cirrus clouds, *J. Appl. Meteor.*, *37*, 184–205.
- Evans, K. F., J. R. Wang, P. E. Racette, G. Heymsfield, and L. Li, (2005), Ice cloud retrievals and analysis with the compact scanning submillimeter imaging radiometer and the cloud radar system during CRYSTAL FACE. *J. Appl. Meteor.*, *44*, 839–859.
- Ferraro R. R., F. Weng, N. C. Grody, L. Zhao, H. Meng, C. Kongoli, P. Pellegrino, S. Qiu, and C. Dean, (2005), NOAA operational hydrological products derived from the advanced microwave sounding unit. *IEEE Trans. Geosci. Remote Sens.*, *43*, 1036–1049.
- Gasiewski, A. J. (1993), Microwave radiative transfer in hydrometeors, in *Atmospheric Remote Sensing by Microwave Radiometry*, edited by M. A. Janssen, pp. 91–144, John Wiley and Sons, New York.
- Grenfell, T. C., and S. G. Warren (1999), Representation of a nonspherical ice particle by a collection of independent spheres for scattering and absorption of radiation, *J. Geophys. Res.*, *104*, 31,697–31,709.
- Hou, A. Y., G. Skofronick-Jackson, C. Kummerow, and J. M. Shepherd (2008), Global Precipitation Measurement, Chapter 6 in Precipitation: Advances in Measurement, Estimation and Prediction Editor: Silas Michaelides, Springer-Verlag, March 2008, 540pp, ISBN: 978-3-540-77654-3.

- Jackson, D.M. and Gasiewski, A.J. (1995), Millimeter-wave radiometric observations of the troposphere: a comparison of measurements and calculations based on radiosonde and Raman lidar, *Geoscience and Remote Sensing, IEEE Transactions on* , vol.33, no.1, pp.3-14, doi: 10.1109/36.368227.
- Kawanishi, T., T. Sezai, Y. Ito, K. Imaoka, T. Takeshima, Y. Ishido, A. Shibata, M. Miura, H. Inahata, and R. W. Spencer (2003), The Advanced Microwave Scanning Radiometer for the Earth Observing System (AMSR-E), NASDA's contribution to the EOS for global energy and water cycle studies, *IEEE Trans. Geosci. Remote Sens.*, 41(2),. 184-194.
- Kim, M.-J., J. A. Weinman, W. S. Olson, D.-E. Chang, G. Skofronick-Jackson, and J. R. Wang (2008), A physical model to estimate snowfall over land using AMSU-B observations, *J. Geophys. Res.*, 113, D09201, doi:10.1029/2007JD008589.
- Kongoli, C., P. Pellegrino, R. Ferraro, N. Grody and H. Meng (2003), A new snowfall detection algorithm over land using measurements from the Advanced Microwave Sounding Unit (AMSU), *Geophys. Res. Lett.*, 30(14) doi:10.1029/2003GL017177.
- Kummerow, Christian, William Barnes, Toshiaki Kozu, James Shiue, Joanne Simpson, (1998) The Tropical Rainfall Measuring Mission (TRMM) Sensor Package. *Journal of Atmospheric and Oceanic Technology*: Vol. 15, No. 3, pp. 809–817.
- Kummerow, C., et al., (2000), The status of the Tropical Rainfall Measuring Mission (TRMM) after two years in orbit, *J. Appl. Meteorol.*, 39, 1965-1982.
- Kummerow, C., S. Finn, J. Crook, D. Randel and W. Berg (2009), An observationally based a-priori database for Bayesian rainfall retrievals, to be submitted to *J. Appl. Meteorol. Climatol.*.
- L'Ecuyer, T. S., P. Gabriel, K. Leesman, S. J. Cooper, and G. L. Stephens, (2006) Objective assessment of the information content of visible and infrared radiance measurements for cloud microphysical property retrievals over the global oceans. Part I: Liquid clouds, *J. Appl. Meteorol. Climatol.*, 45, 20–41.
- Lenoble, J. (1985) *Radiative Transfer in Scattering and Absorbing Atmospheres: Standard Computational Procedures*, A. Deepak Publishing Co, Hampton, VA.
- Lin, X., and A. Y. Hou, (2008), Evaluation of coincident passive microwave rainfall estimates using TRMM PR and ground-based measurements as references, *J. Appl. Meteorol. Climatol.*, 47, 3170-3187.

- Liu, G., 2004: Approximation of single scattering properties of ice and snow particles for high microwave frequencies. *J. Atmospheric Sci.*, 61, 2441–2456.
- Marshall, J. S. and W. M. Palmer (1948), The distribution of raindrops with size, *J. Meteor.*, 5, 165-166.
- Noh, Y.-J., G. Liu, A. S. Jones, and T. H. Vonder Haar (2009), Toward snowfall retrieval over land by combining satellite and in situ measurements, *J. Geophys. Res.*, 114, D24205, doi:10.1029/2009JD012307.
- Sekhon, R. S. and R. C. Srivastava, (1970), Snow size spectra and radar reflectivity, *J. Atmos. Sci.*, 28, 944-983.
- Shi, J. J., W.-K. Tao, T. Matsui, R. Cifelli, A. Hou, S. Lang, A. Tokay, C. Peters-Lidard, G. Skofronick-Jackson, S. Rutledge, and W. Petersen (2009), WRF Simulations of the 20-22 January 2007 Snow Events over Eastern Canada: Comparison with in-situ and Satellite Observations, Submitted to *J. Appl. Meteorol. Climatol.*
- Skofronick-Jackson, G. M.-J. Kim, J. A. Weinman, and D. E. Chang (2004), A physical model to determine snowfall over land by microwave radiometry, *IEEE Trans. Geosci. Remote Sens.*, 42, 1047–1058.
- Skofronick-Jackson, G. A. Heymsfield, E. Holthaus, C. Albers, and M.-J. Kim (2008), Nonspherical and spherical characterization of ice in Hurricane Erin for wideband passive microwave comparisons, *J. Geophys. Res.*, 113, D06201, doi:10.1029/2007JD008866.
- Skofronick-Jackson, G., A. J. Gasiewski, and J. R. Wang (2002), Influence of microphysical cloud parameterizations on microwave brightness temperatures,” *IEEE Trans. Geosci. Remote Sens.*, 40, 187-196.
- Stephens, G. L., et al. (2008), The CloudSat Mission: Performance and early science after the first year of operation, *J. Geophys. Res.*, 113, D00A18, doi:10.1029/2008JD009982.
- Voronovich, A. G. and A. J. Gasiewski (2004), A fast multistream scattering-based Jacobian for microwave radiance assimilation, *IEEE Trans. Geosci. Remote Sens.*, 42, 1749-1761.
- Wu, L., S. A. Braun, J. Halverson, G. Heymsfield (2006), A Numerical Study of Hurricane Erin (2001). Part I: Model Verification and Storm Evolution, *J. Atmos. Sci.*, 63, 65-86.

Figure Captions:

Figure 1: The IWP in  $\text{kg m}^{-2}$  for the (a) MM5 March 2001 blizzard, (b) the 20 January 2007 lake effect snow storm, and (c) the 22 January 2007 synoptic snow event.

Figure 2: Vertical profiles of hydrometeor liquid and ice water contents (upper plots) and the temperature and relative humidity (lower plots) for the anvil, heavy rain, light rain, heavy snow and light snow cases.

Figure 3: For this work, the (a) dendrite particle shape used for snow particles, and (b) the six-bullet rosette shape used for graupel particles. The non-precipitating cloud ice is assumed spherical. (From *Liu*, 2004)

Figure 4: Coefficients for absorption (solid lines) and scattering (dashed lines) for liquid rain, dendritic snow, six-bullet rosettes, solid ice spheres, and fluffy ice spheres (10% ice, 90% air) for hydrometeor contents of (a)  $0.01 \text{ g m}^{-3}$ , (b)  $0.1 \text{ g m}^{-3}$ , (c)  $0.5 \text{ g m}^{-3}$ , and (d)  $0.75 \text{ g m}^{-3}$ .

Figure 5: Temperature weighting vectors  $\mathbf{W}_{\text{ALL}}(z_i)T(z_i)$  for the nadir-viewed anvil, heavy rain, light rain, heavy snow, and light snow cases. Upper panels are for TRMM frequencies (10-89 GHz), middle panels are for AMSU-B frequencies (89-183 $\pm$ 7 GHz), and lower panels for the submillimeter-wave channels (325-874 GHz).

Figure 6: Brightness temperature values using a standard clear-air winter atmosphere profile for varying surface emissivities and surface temperatures at (a) 10 GHz, (b) 37 GHz, (c) 89 GHz, (d) 166 GHz, (e) 183 $\pm$ 3 GHz, and (f) 183 $\pm$ 7 GHz. The X-axis indicates the values used for surface emissivity, while the colored lines indicate surface temperature.

Figure 7: Percentage contributions from the surface (green), the hydrometeors (red), the relative humidity (light blue), the cosmic background (<1% for all channels except 10 GHz where it is 1.3%)+cloud water+cloud ice (purple), and the atmospheric oxygen and nitrogen (gray) to the resultant nadir brightness temperatures for (a) the heavy rain over ocean case, (b) the light rain over land case, and (c) the anvil profile case.

Figure 8: Similar to Fig. 7, percentage contributions for the single profile (a) heavy snow, (b) moderate snow, and (c) light snow cases.

Figure 9: Similar to Fig. 7, percentage contributions averaged over IWP of 0.5 to  $1.0 \text{ kg m}^{-2}$  for the (a) WRF 20 January 2007 lake effect case and (b) the WRF for 22 January 2007.

Figure 10: Similar to Fig. 7, percentage contributions of a March 2001 snow blizzard MM5 simulation averaged over (a) IWP of 0.5 to  $1.0 \text{ kg m}^{-2}$  and (b) IWP of 9.5 to  $10.0 \text{ kg m}^{-2}$ .

682

TABLE I. SURFACE CONDITIONS FOR THE CASE PROFILES.

Profile	Type	Conditions	T (°C)	RH (%)	Liquid Surface Rate (mm hr <sup>-1</sup> )	LWP (kg m <sup>-2</sup> )	IWP (kg m <sup>-2</sup> )
Heavy Rain	Ocean	Calm Winds	22.5	100.0	25.0	5.37	1.77
Light Rain	Land	Forested	23.1	95.2	0.5	0.49	0.83
Anvil	Ocean	Calm Winds	23.1	88.9	0.0	0.0	0.28
Light Snow	Land	Deep dry snow	-6	93.8	0.5	0.0	0.32
Moderate Snow	Land	Deep dry snow	-6	93.8	2.5	0.0	0.94
Heavy Snow	Land	Deep dry snow	-6	93.8	15.7	0.0	4.24

683

684

685

686

687

TABLE II. BRIGHTNESS TEMPERATURES FOR THE HEAVY, MODERATE, AND LIGHT SNOW CASES AND THE HEAVY RAIN, LIGHT RAIN, AND ANVIL PROFILES FOR “ALL” HYDROMETEORS INCLUDED AND CLEAR AIR “CA” CONDITIONS.

Freq. GHz	Heavy Snow Over Land		Moderate Snow Over Land	Light Snow Over Land	Heavy Rain Over Ocean		Light Rain Over Land		Anvil Over Ocean	
Case	All	CA	All	All	All	CA	All	CA	All	CA
10	217.1	216.7	216.8	222.4	212.0	121.9	286.5	286.5	121.4	121.4
19	189.0	188.5	188.4	189.4	266.1	165.0	295.1	296.1	159.3	159.6
21	196.1	196.1	197.7	198.0	268.2	205.4	289.6	290.2	195.5	196.4
37	184.8	178.6	181.8	175.2	250.0	178.2	289.5	294.1	173.1	173.1
89	216.2	199.0	207.7	199.2	192.7	255.5	271.5	291.9	247.6	247.7
166	206.0	252.2	247.4	250.9	174.7	278.5	250.2	279.6	278.7	280.4
183±1	240.8	242.8	243.0	242.0	232.6	242.5	240.6	242.5	241.3	243.1
183±3	239.3	252.3	250.0	253.7	223.4	254.6	249.2	254.8	256.5	255.5
183±7	225.0	260.9	253.5	256.2	196.0	266.7	250.6	267.2	267.5	268.4
325±7.0	211.8	258.4	242.7	253.0	191.2	262.2	229.6	262.7	256.8	263.8
325±9.5	208.1	259.9	241.2	252.0	189.0	264.4	227.0	264.9	258.5	266.1
448±1.5	229.1	231.6	223.3	230.9	216.9	232.3	227.4	232.1	232.1	233.1
448±7.2	226.92	244.4	236.4	240.7	203.4	247.2	232.4	247.2	241.6	247.6
642	227.6	245.0	237.7	235.3	206.4	248.2	229.3	248.2	237.7	248.6
874	230.0	246.3	237.4	239.9	210.3	249.9	227.6	249.9	234.1	250.4

691

TABLE III. PERCENTAGES FOR THE HEAVY RAIN, LIGHT RAIN, AND ANVIL CASES AT A 53° VIEWING ANGLE. NOTE THAT THE PERCENTAGES FOR V AND H POLARIZATION FOR LIGHT RAIN OVER LAND ARE THE SAME SINCE THE LAND SURFACE IS NOT POLARIZED.

Freq. [GHz]	Heavy Rain over Ocean V-pol			Heavy Rain over Ocean H-pol			Light Rain over Land V-pol			Light Rain over Land H-pol			Anvil over Ocean V-pol			Anvil over Ocean H-pol		
	surf	hydr	RH	surf	hydr	RH	surf	hydr	RH	surf	hydr	RH	surf	hydr	RH	surf	hydr	RH
10	33	64	2	16	81	2	96	1	2	96	1	2	93	0	4	82	0	10
19	5	87	8	2	89	8	76	5	17	76	5	17	66	0	31	41	0	53
21	2	79	18	1	80	18	56	6	37	56	6	37	45	0	53	23	0	73
37	0.1	96	2	0.1	96	2	64	19	13	64	19	13	67	0	24	43	0	42
89	0	95	2	0	95	2	14	56	26	14	56	26	34	0	59	18	1	73
166	0	93	4	0	93	4	0.3	63	35	0.3	63	35	1	3	94	1	3	94
183±1	0	51	47	0	51	47	0	11	86	0	11	86	0	3	95	0	3	95
183±3	0	78	20	0	78	20	0	35	62	0	35	62	0	5	92	0	5	92
183±7	0	89	8	0	89	8	0	55	42	0	55	42	0	5	92	0	5	92
325±7.0	0	87	7	0	87	7	0	75	19	0	75	19	0	17	78	0	17	78
325±9.5	0	87	6	0	87	6	0	77	18	0	77	18	0	16	79	0	16	79
448±1.5	0	48	47	0	48	47	0	14	82	0	14	82	0	8	88	0	8	88
448±7.2	0	68	18	0	68	18	0	53	38	0	53	38	0	28	62	0	28	62
642	0	68	13	0	68	13	0	58	28	0	58	28	0	38	48	0	38	48
874	0	69	7	0	69	7	0	59	19	0	59	19	0	42	34	0	42	34

696

697 TABLE IV. PERCENTAGES FOR THE HEAVY, MODERATE, AND LIGHT SNOW CASES AT A NADIR AND  
 698 53° VIEWING ANGLE. NOTE THAT THE PERCENTAGES FOR V AND H POLARIZATION ARE THE SAME.

	Nadir Viewing Angle									53° viewing angle								
Freq. [GHz]	Heavy Snow over Land			Moderate Snow over Land			Light Snow over Land			Heavy Snow over Land			Moderate Snow over Land			Light Snow over Land		
Source	surf	hydr	RH	surf	hydr	RH	surf	hydro	RH	surf	hydr	RH	surf	hydr	RH	surf	hydr	RH
<b>10</b>	97	<b>2</b>	0	98	<b>0</b>	0	98	<b>0</b>	0	95	<b>3</b>	0	97	<b>0</b>	0	97	<b>0</b>	0
<b>19</b>	91	<b>5</b>	3	92	<b>0</b>	5	93	<b>0</b>	5	86	<b>8</b>	4	88	<b>1</b>	7	88	<b>1</b>	7
<b>21</b>	84	<b>7</b>	8	86	<b>1</b>	11	86	<b>0</b>	11	76	<b>10</b>	12	79	<b>1</b>	17	79	<b>1</b>	17
<b>37</b>	84	<b>11</b>	1	87	<b>2</b>	4	86	<b>2</b>	4	77	<b>16</b>	2	80	<b>3</b>	6	79	<b>2</b>	6
<b>89</b>	58	<b>37</b>	2	71	<b>8</b>	13	71	<b>6</b>	15	45	<b>48</b>	3	59	<b>11</b>	19	59	<b>9</b>	21
<b>166</b>	13	<b>80</b>	6	41	<b>13</b>	44	42	<b>8</b>	48	10	<b>82</b>	6	25	<b>16</b>	56	26	<b>10</b>	61
<b>183±1</b>	0	<b>36</b>	63	0	<b>1</b>	98	0	<b>0</b>	99	0	<b>31</b>	68	0	<b>1</b>	97	0	<b>0</b>	98
<b>183±3</b>	0	<b>63</b>	36	0	<b>3</b>	96	0	<b>1</b>	98	0	<b>62</b>	36	0	<b>3</b>	95	0	<b>0</b>	97
<b>183±7</b>	2	<b>82</b>	16	8	<b>7</b>	83	9	<b>4</b>	86	1	<b>82</b>	15	2	<b>7</b>	88	2	<b>3</b>	92
<b>325±7.0</b>	2	<b>88</b>	8	2	<b>14</b>	81	2	<b>5</b>	90	2	<b>87</b>	8	0	<b>17</b>	78	0	<b>5</b>	89
<b>325±9.5</b>	3	<b>88</b>	6	3	<b>16</b>	77	0	<b>6</b>	86	3	<b>87</b>	6	1	<b>18</b>	76	1	<b>6</b>	88
<b>448±1.5</b>	0	<b>17</b>	81	0	<b>3</b>	94	0	<b>0</b>	96	0	<b>14</b>	83	0	<b>3</b>	93	0	<b>0</b>	96
<b>448±7.2</b>	0	<b>56</b>	40	0	<b>16</b>	79	0	<b>3</b>	91	0	<b>57</b>	37	0	<b>18</b>	73	0	<b>3</b>	88
<b>642</b>	0	<b>58</b>	37	0	<b>24</b>	68	0	<b>6</b>	83	0	<b>58</b>	33	0	<b>27</b>	60	0	<b>7</b>	78
<b>874</b>	0	<b>60</b>	30	0	<b>29</b>	56	0	<b>11</b>	70	0	<b>59</b>	25	0	<b>32</b>	45	0	<b>13</b>	60

699

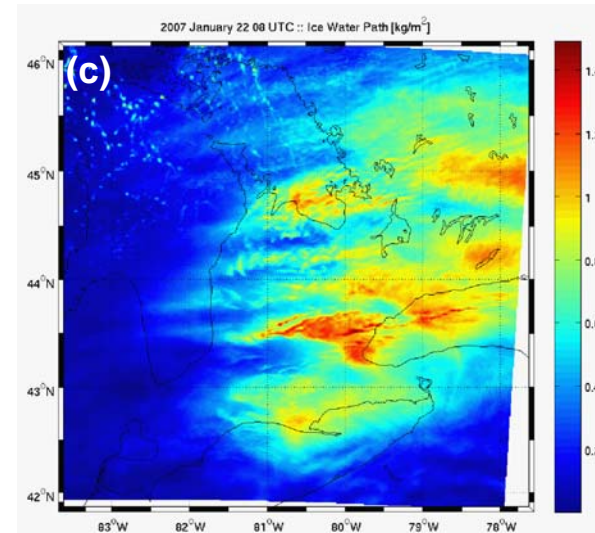
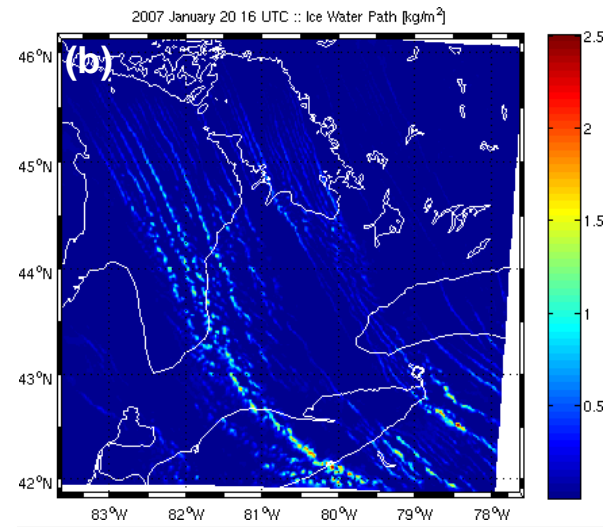
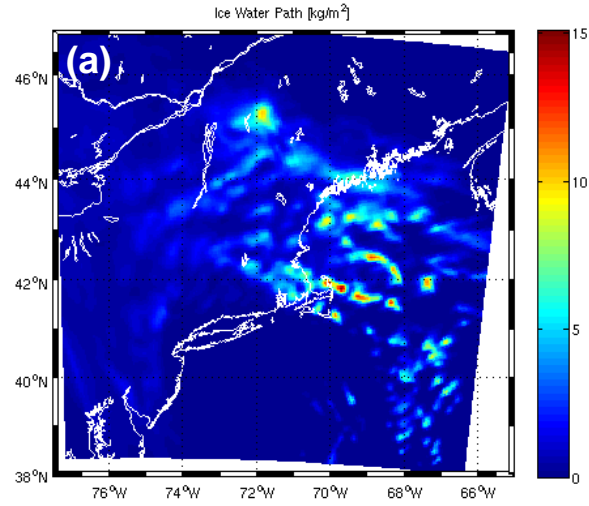


Figure 1: The IWP in  $\text{kg m}^{-2}$  for the (a) MM5 March 2001 blizzard, (b) the 20 January 2007 lake effect snow storm, and (c) the 22 January 2007 synoptic snow event.



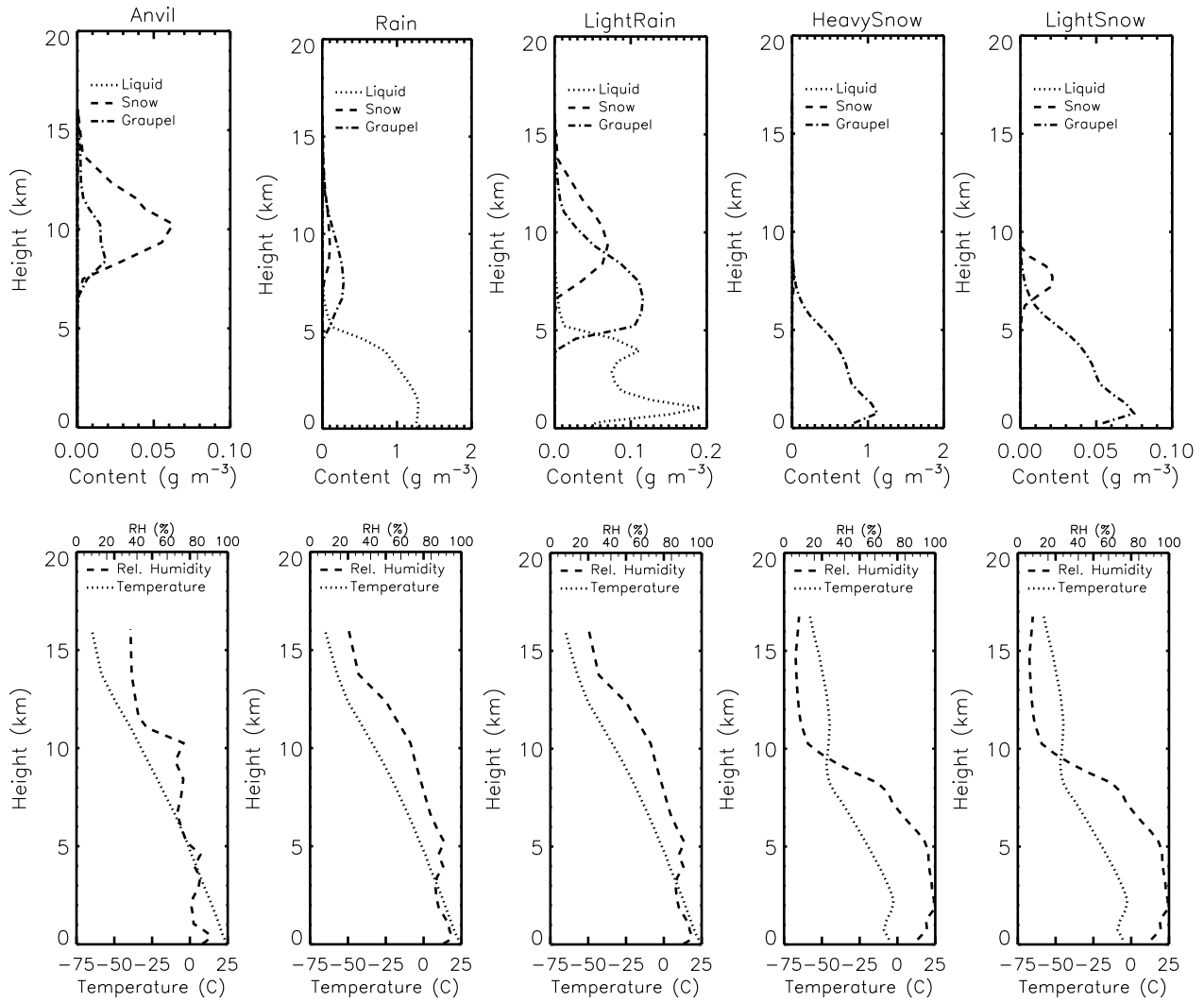


Figure 2: Vertical profiles of hydrometeor liquid and ice water contents (upper plots) and the temperature and relative humidity (lower plots) for the anvil, heavy rain, light rain, heavy snow and light snow cases.

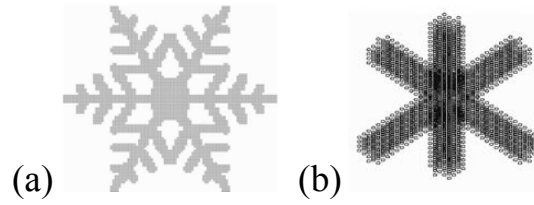


Figure 3: For this work, the (a) dendrite particle shape used for snow particles, and (b) the six-bullet rosette shape used for graupel particles. The non-precipitating cloud ice is assumed spherical. (From *Liu, 2004*)

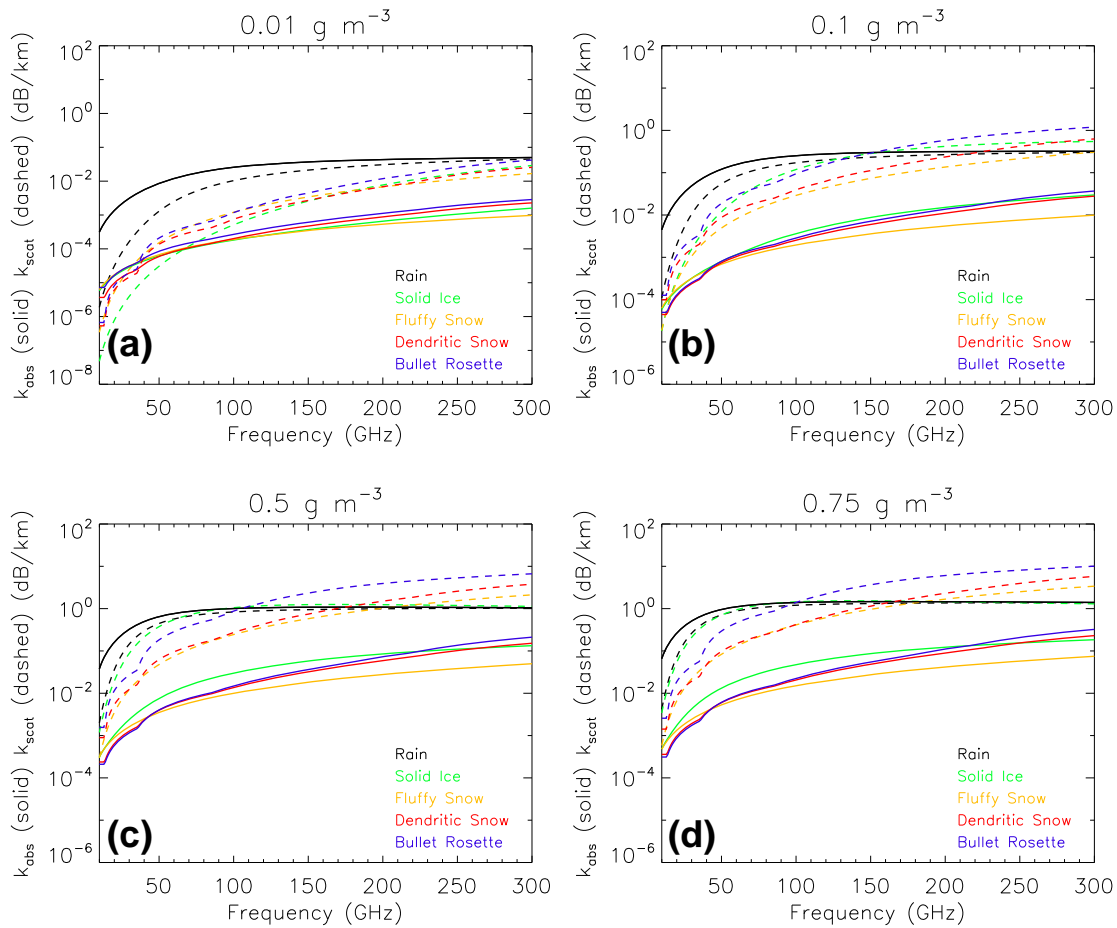


Figure 4: Coefficients for absorption (solid lines) and scattering (dashed lines) for liquid rain, dendritic snow, six-bullet rosettes, solid ice spheres, and fluffy ice spheres (10% ice, 90% air) for hydrometeor contents of (a)  $0.01 \text{ g m}^{-3}$ , (b)  $0.1 \text{ g m}^{-3}$ , (c)  $0.5 \text{ g m}^{-3}$ , and (d)  $0.75 \text{ g m}^{-3}$ .

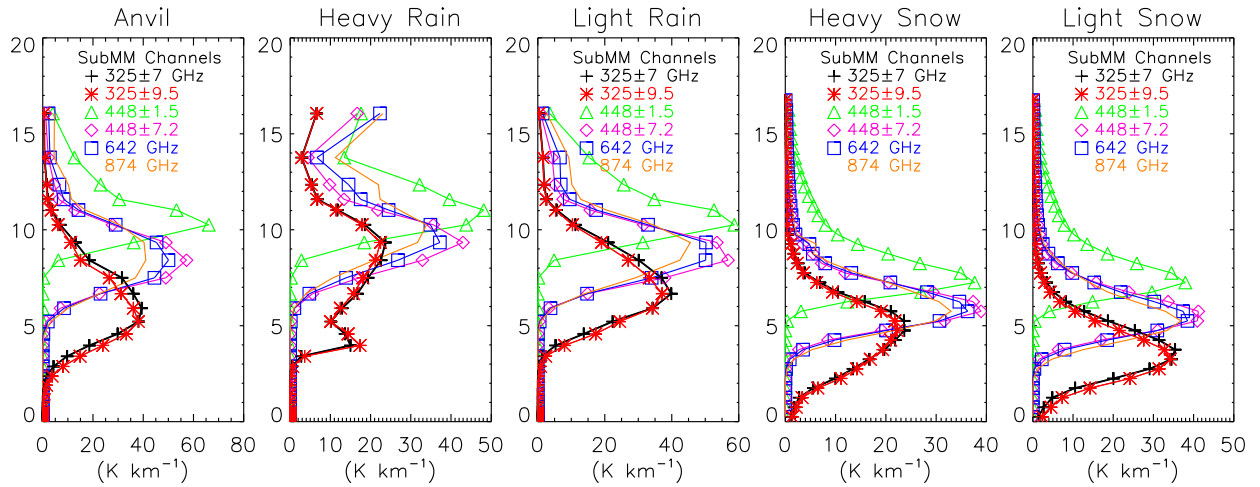
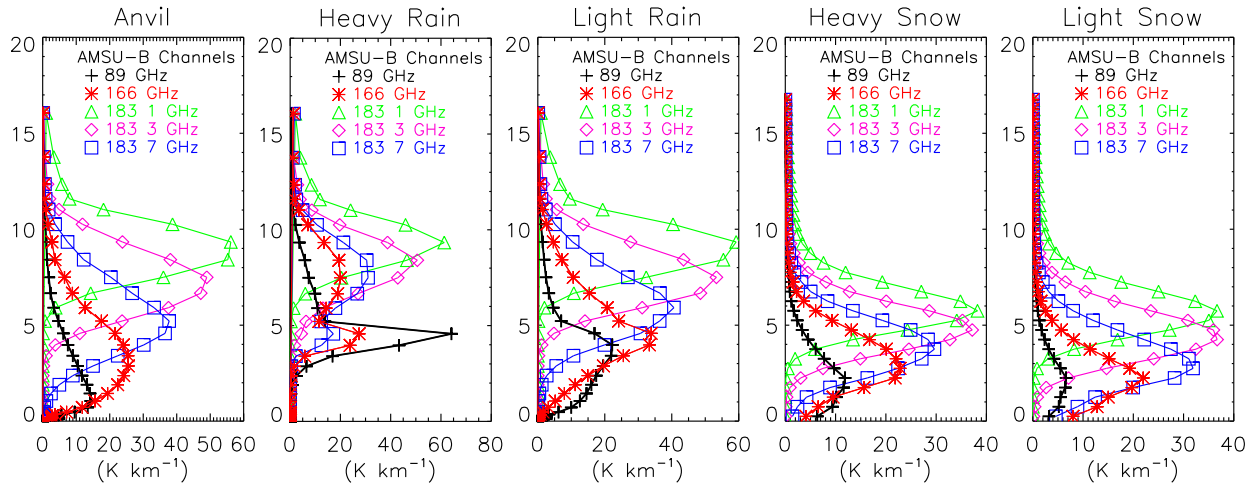
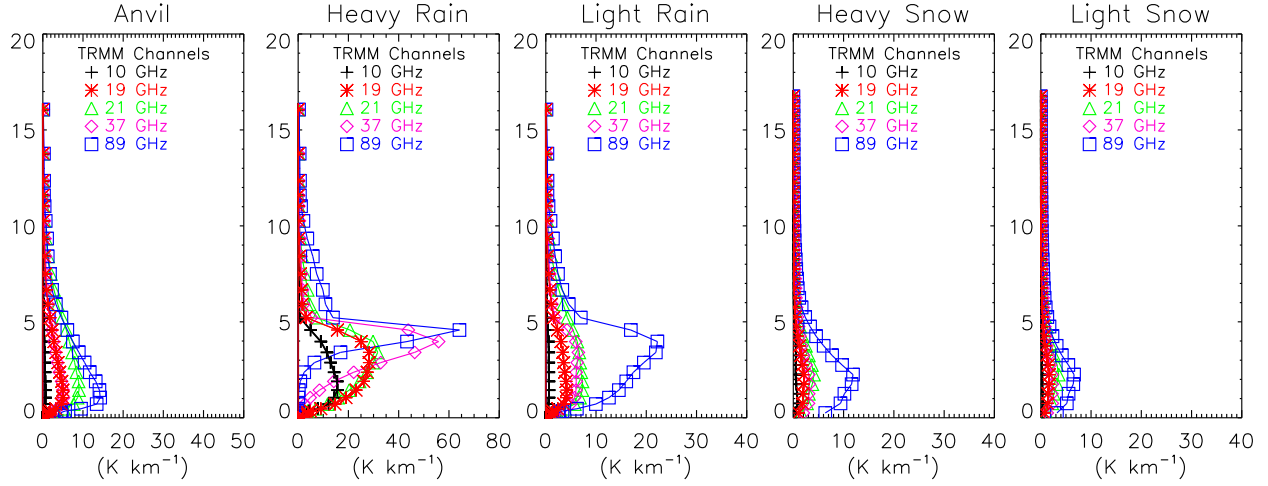
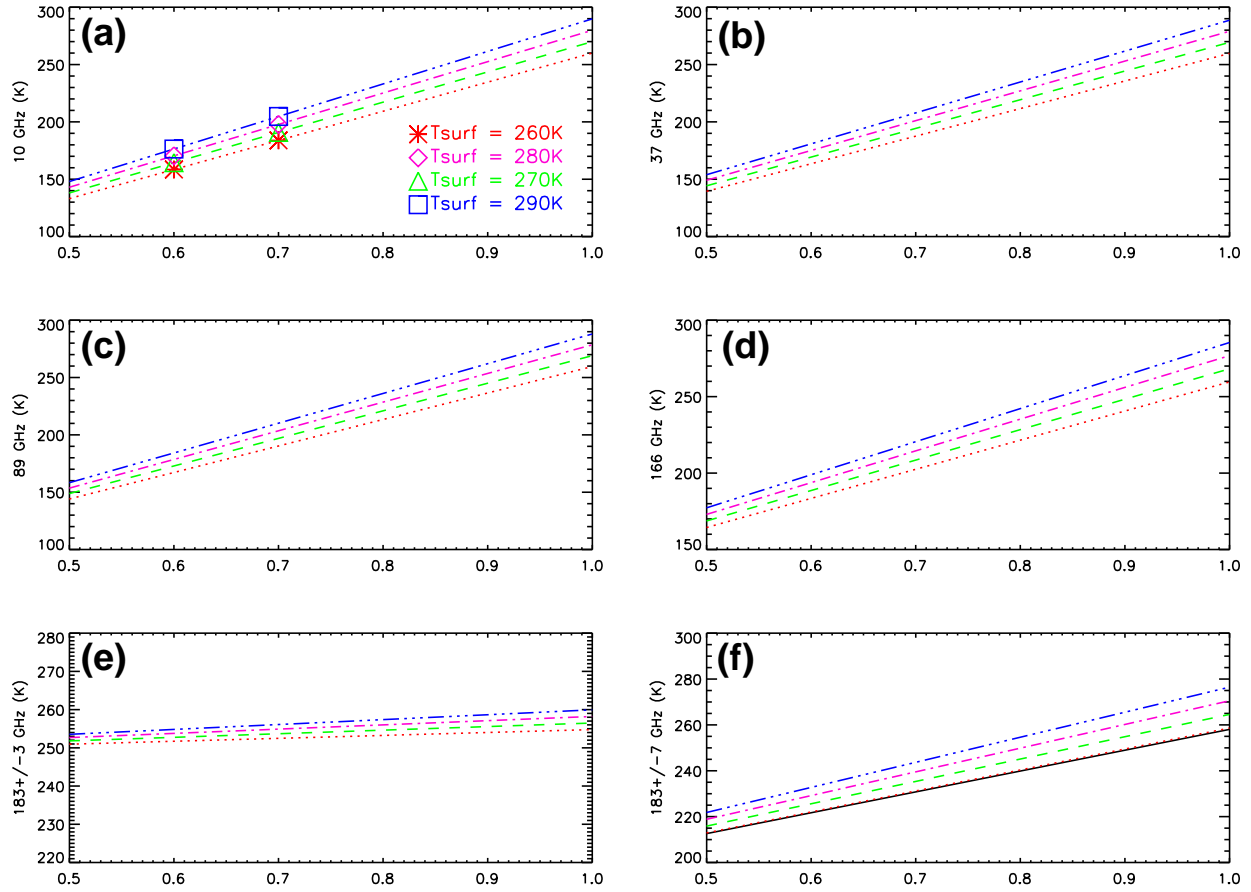


Figure 5: Temperature weighting vectors  $\mathbf{W}_{\text{ALL}}(z_i)T(z_i)$  for the nadir-viewed anvil, heavy rain, light rain, heavy snow, and light snow cases. Upper panels are for TRMM frequencies (10-89 GHz), middle panels are for AMSU-B frequencies (89-183±7 GHz), and lower panels for the submillimeter-wave channels (325-874 GHz).

744



745

746

747 Figure 6: Brightness temperature values using a standard clear-air winter atmosphere profile for  
 748 varying surface emissivities and surface temperatures at (a) 10 GHz, (b) 37 GHz, (c) 89 GHz, (d)  
 749 166 GHz, (e)  $183\pm 3$  GHz, and (f)  $183\pm 7$  GHz. The X-axis indicates the values used for surface  
 750 emissivity, while the colored lines indicate surface temperature.

751

752

753

754

755

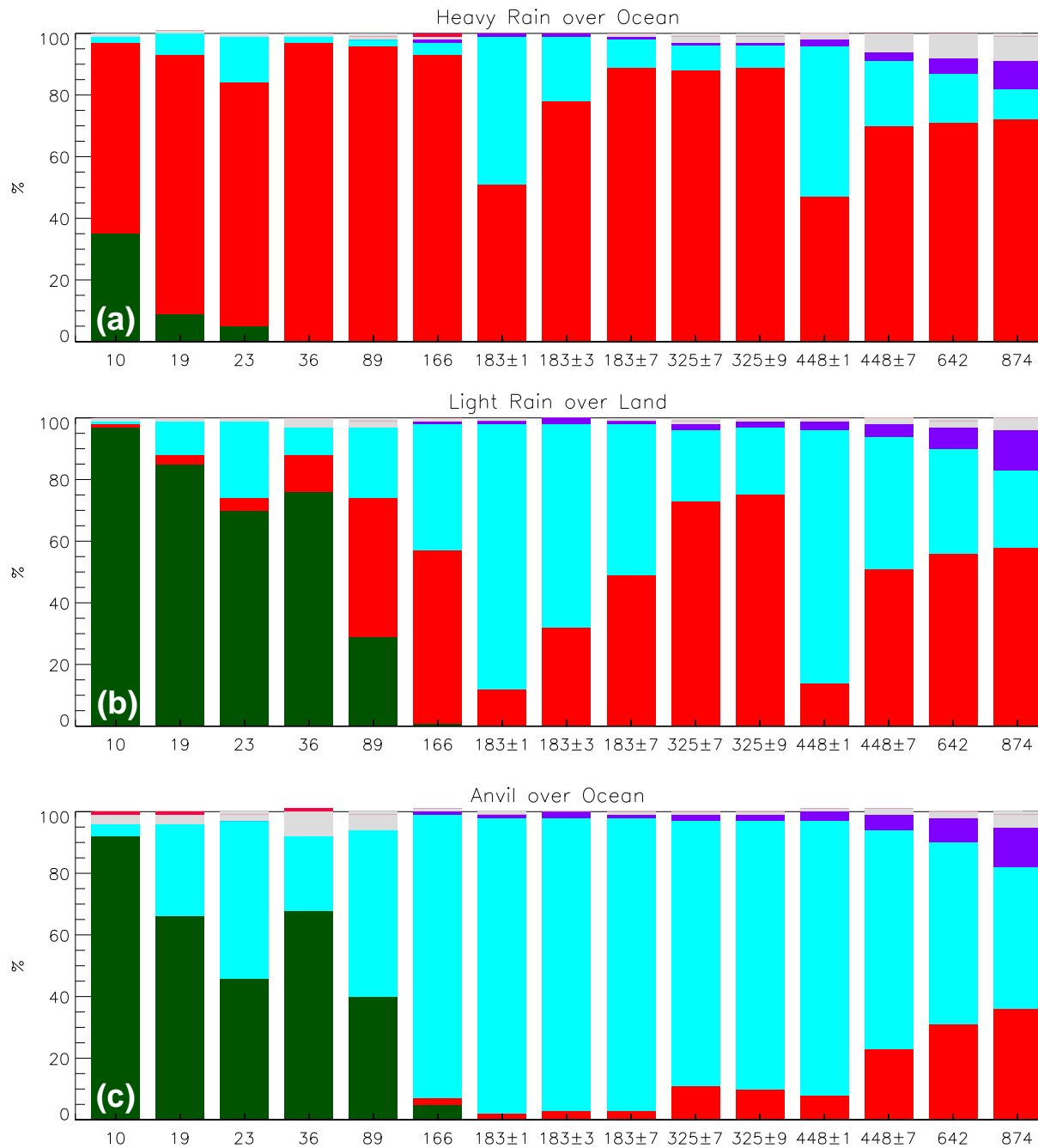


Figure 7: Percentage contributions from the surface (green), the hydrometeors (red), the relative humidity (light blue), the cosmic background (<1% for all channels except 10 GHz where it is 1.3%)+cloud water+cloud ice (purple), and the atmospheric oxygen and nitrogen (gray) to the resultant nadir brightness temperatures for (a) the heavy rain over ocean case, (b) the light rain over land case, and (c) the anvil profile case.

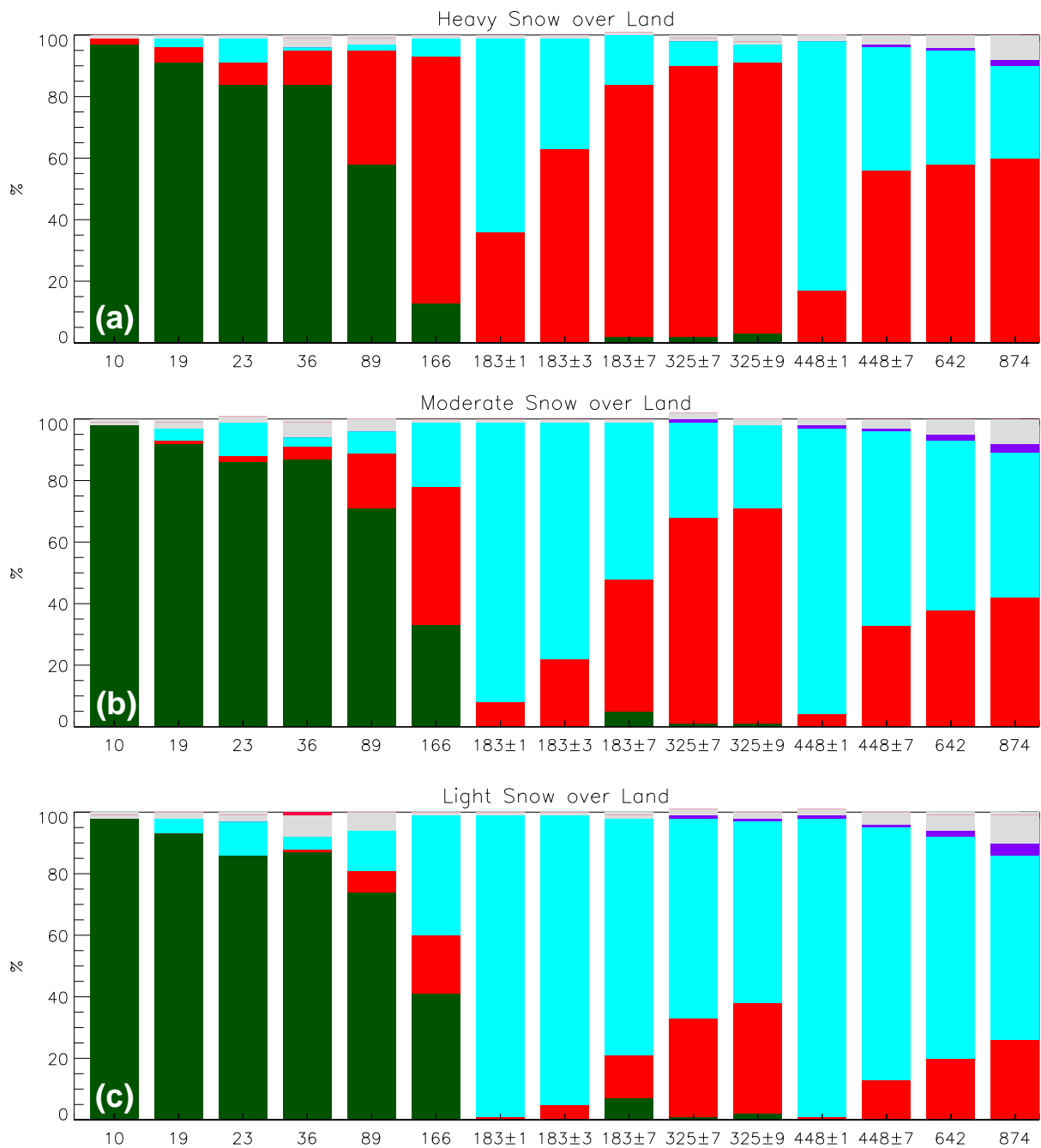


Figure 8: Similar to Fig. 7, percentage contributions for the single profile (a) heavy snow, (b) moderate snow, and (c) light snow cases.

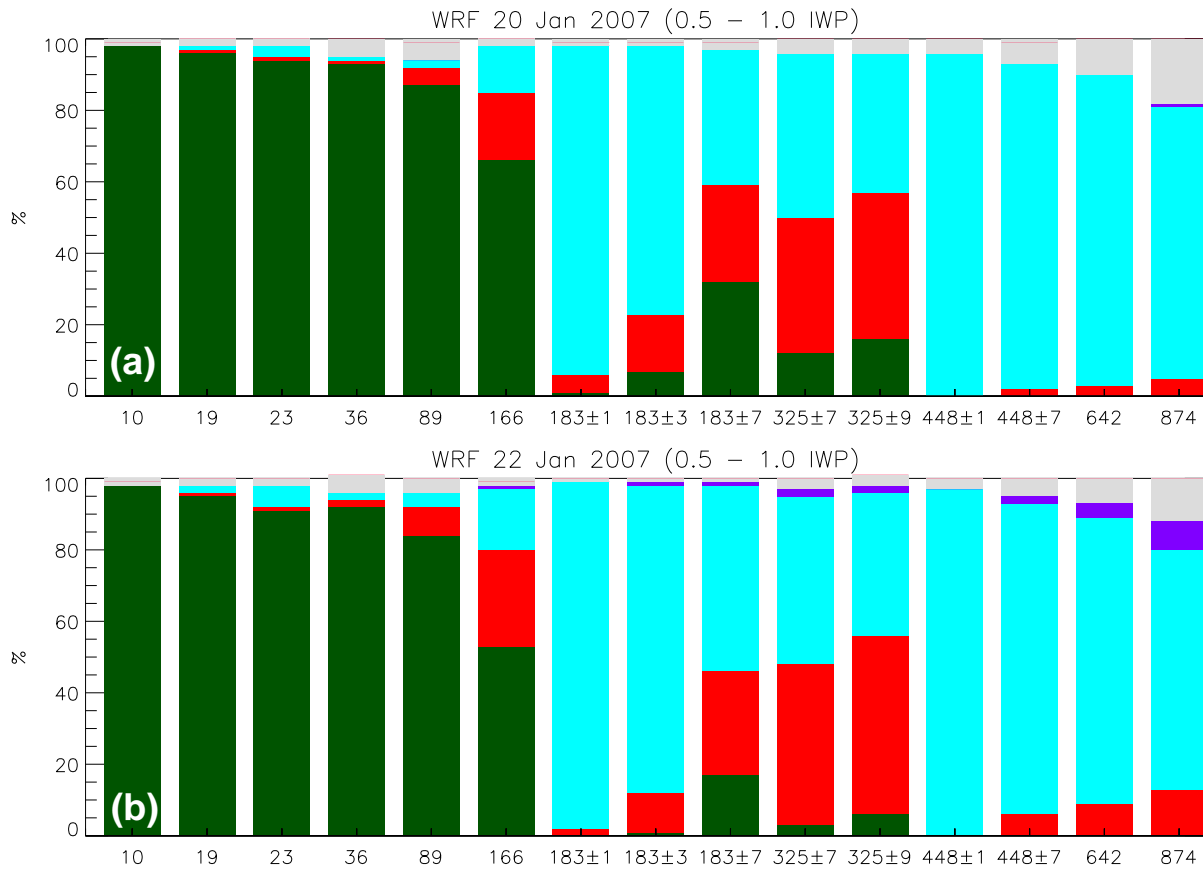


Figure 9: Similar to Fig. 7, percentage contributions averaged over IWP of 0.5 to 1.0  $\text{kg m}^{-2}$  for the (a) WRF 20 January 2007 lake effect case and (b) the WRF for 22 January 2007.

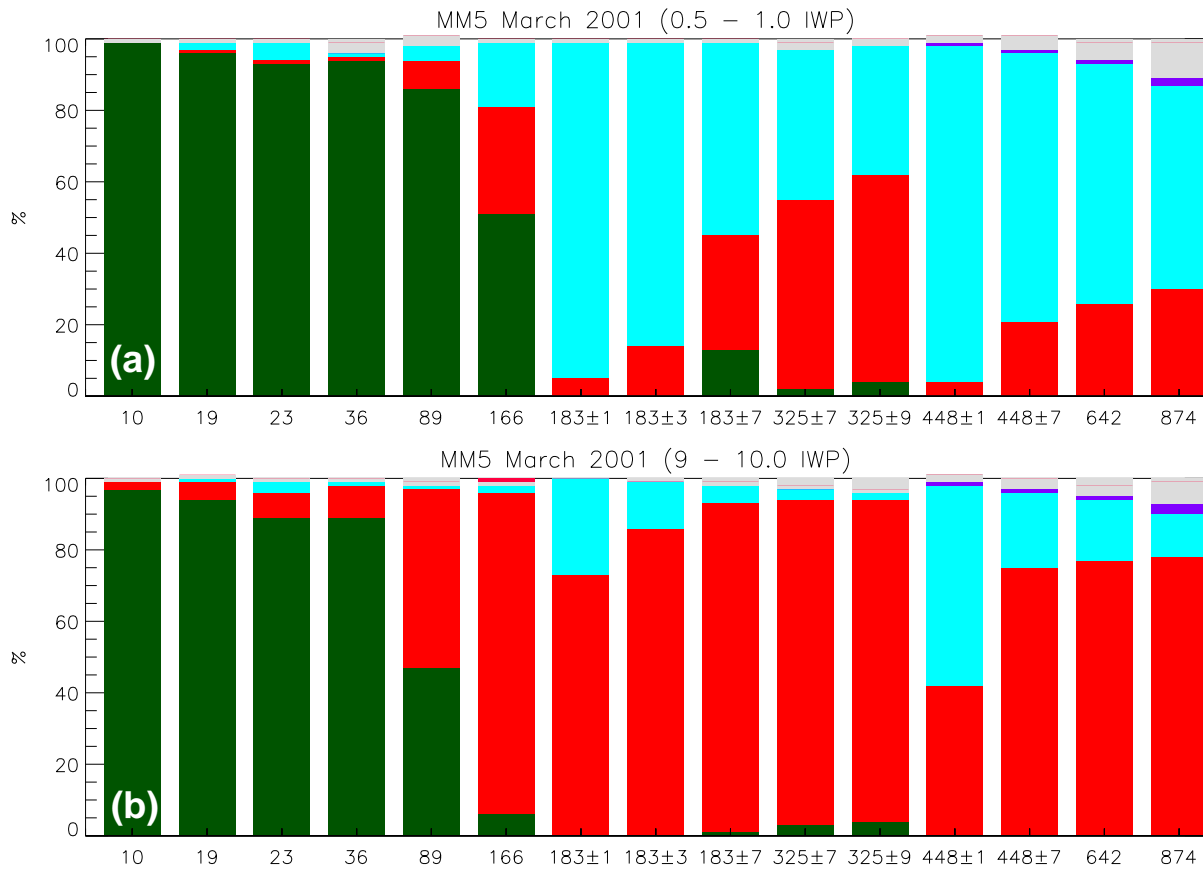


Figure 10: Similar to Fig. 7, percentage contributions of a March 2001 snow blizzard MM5 simulation averaged over (a) IWP of 0.5 to 1.0 kg m<sup>-2</sup> and (b) IWP of 9.5 to 10.0 kg m<sup>-2</sup>.